Epitaxial phase diagrams of $SrTiO_3$, $CaTiO_3$, and $SrHfO_3$: Computational investigation including the role of antiferrodistortive and *A*-site displacement modes

Thomas Angsten* and Mark Asta

Department of Materials Science and Engineering, University of California, Berkeley, Berkeley, California 94720, USA
and Materials Sciences Division, Lawrence Berkeley National Laboratory, Berkeley, California 94720, USA

(Received 31 January 2018; revised manuscript received 26 March 2018; published 5 April 2018)

Ground-state epitaxial phase diagrams are calculated by density functional theory (DFT) for $SrTiO_3$, $CaTiO_3$, and $SrHfO_3$ perovskite-based compounds, accounting for the effects of antiferrodistortive and *A*-site displacement modes. Biaxial strain states corresponding to epitaxial growth of (001)-oriented films are considered, with misfit strains ranging between −4% and 4%. Ground-state structures are determined using a computational procedure in which input structures for DFT optimizations are identified as local minima in expansions of the total energy with respect to strain and soft-mode degrees of freedom. Comparison to results of previous DFT studies demonstrates the effectiveness of the computational approach in predicting ground-state phases. The calculated results show that antiferrodistortive octahedral rotations and associated *A*-site displacement modes act to suppress polarization and reduce the epitaxial strain energy. A projection of calculated atomic displacements in the ground-state epitaxial structures onto soft-mode eigenvectors shows that three ferroelectric and six antiferrodistortive displacement modes are dominant at all misfit strains considered, with the relative contributions from each varying systematically with the strain. Additional *A*-site displacement modes contribute to the atomic displacements in $CaTiO_3$ and $SrHfO_3$, which serve to optimize the coordination of the undersized *A*-site cation.

DOI: 10.1103/PhysRevB.97.134103

I. INTRODUCTION

Ferroelectric thin films based on perovskite-structured oxide compounds are widely researched for a variety of microelectronic device applications [1]. Thin-film forms of these ferroelectric (FE) materials are of interest due to their reduced dimensionality, as well as the novel properties that arise from epitaxial constraints [2]. In particular, epitaxial strain has been shown to have a strong effect on the polarization and domain behavior of FEs [3], and it thus provides a means of tuning properties for device applications.

To exploit such epitaxial effects, predictive first-principles computational models based on density-functional theory (DFT) have been developed and applied to predict the structure and polarization of oxide FEs as a function of the biaxial strain. In such modeling efforts, a few approaches have been employed. In early studies [4,5], expansions of the total energy with respect to the amplitudes of unstable phonon modes and strain were determined and used to compute stable structures and associated energetics and polarizations as a function of the misfit strain. Although effective for prototypical perovskites like $BaTiO_3$, a limitation of the approach was the consideration of only zone-centered soft-phonon modes and the associated neglect of octahedral rotations, which have been shown to suppress polarization in many perovskites [6]. In more recent studies that have considered a broader range of compositions [7–12], direct DFT relaxations of candidate perovskite-based structures were undertaken as a function of the biaxial strain. In some of these studies, candidate structures were limited to those that could be derived only from distortions and zone-center displacements in the primitive five-atom unit cell, again neglecting structural distortions associated with octahedral rotations. In other first-principles computational studies, more complex structures have been considered, derived from experimental measurements [13,14]. The latter studies have accounted for important effects of non-zone-centered displacement modes, such as antiferrodistortive (AFD) octahedral rotations or *A*-site displacement modes, but they have been limited to the relatively few compositions where experimentally measured crystallographic data for strained thin films are available.

In the present work, a methodology is presented extending previous efforts to account for non-zone-centered modes in the calculation of ground-state structures and associated polarizations in epitaxially strained perovskite thin films. The approach makes use of direct DFT optimizations of candidate structures corresponding to local minima in expansions of the energy with respect to the strain and the amplitudes of the nine most unstable phonon modes of reference high-symmetry perovskite structures. Expansions are carried out at several strain states, and the full set of structures corresponding to the minima identified in the energy expansions is used as input to DFT energy minimizations as a function of the biaxial strain. From the lowest-energy structures identified, epitaxial phase diagrams and polarization plots similar to those presented in Ref. [8] are constructed, but accounting for more complex polymorphs that feature non-zone-centered displacement modes.

This approach is employed in the present work in a DFT-based study of the ground-state phase diagrams of epitaxially strained $SrTiO_3$, $CaTiO_3$, and $SrHfO_3$ compounds. While

*angsten@berkeley.edu

$SrTiO_3$ and $CaTiO_3$ are more commonly studied perovskite oxides and thus serve as good reference compounds for comparisons to other methods, $SrHfO_3$ is a lesser-studied system in the context of thin films. $SrHfO_3$ was chosen due to its similarity to $CaTiO_3$ with respect to ratios of ionic radii, thus facilitating an analysis of the effect of composition on thin-film properties, but also because of its promising polar response properties. In Ref. [15], a metastable $P4mm$ phase of $SrHfO_3$ was selected out of a first-principles screening of nearly a thousand piezoelectric tensors due to its large piezoelectric response, having a maximal longitudinal modulus of $||e_{ij}||_{\max} \approx 10\ \mathrm{C/m^2}$. It is thus worthwhile to determine in the present work whether this $P4mm$ $SrHfO_3$ phase can be epitaxially stabilized by measuring its degree of metastability and, also, to see if this system retains a large polarization under epitaxy.

Ground-state structures and associated energetics and polarization properties are calculated for $SrTiO_3$, $CaTiO_3$, and $SrHfO_3$ as a function of the epitaxial strain state, corresponding to the biaxial tension and compression in the (001) plane. In the remainder of this paper, the computational approach is described in detail in Sec. II, and results obtained are presented in Sec. III. Insights derived from these results, as they relate to the role of non-zone-centered phonons in the stability and polarization properties of epitaxially strained perovskite thin films, are discussed in Sec. IV, and the main conclusions are summarized in Sec. V.

II. METHOD

In the present computational approach, epitaxial thin films are modeled as bulk compounds subjected to biaxial strain in the (001) plane, neglecting explicit surface and interface effects. In discussing crystallographic structures and strain states, we employ throughout a coordinate system in which the x and y directions are along the [100] and [010] directions of a reference tetragonally distorted perovskite unit cell, and z is the direction normal to the plane of the biaxial strain. In what follows, a description is given of the nature of the energy expansions used to identify candidate structures for DFT optimizations (Sec. II A), the way in which resulting optimized structures are used to construct epitaxial ground-state phase diagrams (Sec. II B), and the associated details of the DFT calculations (Sec. II C).

A. Total energy expansions

For each composition, the lattice constant of an ideal cubic perovskite structure (space group $Pm\bar{3}m$) is calculated. Tensile strains are then applied to the x and y directions by a misfit strain $\bar{\eta}$, considering values of -2%, -1%, 0%, 1%, and 2%. For each biaxial strain state, the out-of-plane (c-axis) lattice constant is relaxed, and 40-atom ($2 \times 2 \times 2$) supercells are then constructed from these structures to serve as reference states for subsequent expansions of the total energy.

The total energy expansions consider both homogeneous strain and atomic displacement degrees of freedom. Regarding strain, the mechanical boundary conditions for a coherently strained epitaxial thin film are defined as

$$\epsilon_{xx} = \epsilon_{yy} = \bar{\eta}, \quad \epsilon_{xy} = 0; \quad \sigma_{zz} = \sigma_{yz} = \sigma_{xz} = 0, \qquad (1)$$

where ϵ and σ are the strain and stress tensors, respectively, and $\bar{\eta}$ is the misfit strain, calculated as $\bar{\eta} = a/a_0 - 1$, where a_0 is the lattice constant of the reference cubic perovskite (with zero misfit strain), and a corresponds to the lattice constant of a cubic substrate. At fixed misfit strain, ϵ_{zz}, ϵ_{xz}, and ϵ_{yz} constitute the three strain degrees of freedom. For the following total energy expansions, the two out-of-plane shear strains ϵ_{xz} and ϵ_{yz} are assumed to be relatively unimportant in dictating candidate energy minima in the potential-energy landscape, and only ϵ_{zz} is considered explicitly.

Regarding the atomic positional degrees of freedom, the most basic approach is to include all x, y, and z displacements of each atom in the reference structure. However, this leads to $(40 \times 3) - 3 = 117$ additional degrees of freedom and a prohibitive number of coefficients that must be evaluated. A more efficient technique is to choose a set of displacement variables that still forms a complete basis but can be prioritized by relative importance for the energy landscape. This is accomplished most simply by considering unstable and soft modes of the force-constant matrix [4].

The force-constant matrix, $D^{\tau,\tau'}_{\alpha,\beta}$, is defined as

$$D^{\tau,\tau'}_{\alpha,\beta} = \left.\frac{\partial^2 E}{\partial \upsilon^{\tau}_{\alpha} \partial \upsilon^{\tau'}_{\beta}}\right|_0. \qquad (2)$$

In this work, $D^{\tau,\tau'}_{\alpha,\beta}$ is always a 120×120 matrix, with $\vec{\upsilon}$ denoting the 120-component atomic displacement vector in Cartesian coordinates, τ and τ' denoting atom indices (1 through 40), and α and β denoting Cartesian indices (x, y, or z). For each composition, a force-constant matrix is calculated for each of the five biaxially strained reference structures defined above.

For each force-constant matrix, the eigenvectors and eigenvalues are determined by the eigenequation:

$$\sum_{\beta\tau'} D^{\tau,\tau'}_{\alpha,\beta} \xi^{\tau'}_{\beta}(j) = \lambda(j) \xi^{\tau}_{\alpha}(j). \qquad (3)$$

Here, j is a mode index running from 1 to 120, $\lambda(j)$ is the jth real-valued eigenvalue, and $\xi(j)$ is the jth 120-component real-valued eigen-displacement vector.

The eigenvectors $\xi(j)$ form a complete orthonormal basis capable of describing any pattern of displacement having wavelengths commensurate with the supercell dimensions. This basis is more convenient than Cartesian coordinates under the assumption that the $\xi(j)$ corresponding to lower $\lambda(j)$ eigenvalues dominate in the lowest-energy structures. Because the eigenvalues $\lambda(j)$ track the curvature of the energy with respect to that displacement mode, very positive curvatures will tend to prohibit the appearance of these displacement modes in low-energy structures.

The vector corresponding to the displacements within the 40-atom supercell can be written in terms of these eigenvectors $\xi(j)$ as

$$\vec{\upsilon} = \sum_j u_j \xi(j). \qquad (4)$$

Here, u_j is the jth eigenmode coordinate, a real-valued scalar whose absolute value, the eigenmode amplitude, represents the degree to which the jth eigenmode displacement pattern,

$\xi(j)$, contributes to the atomic displacements. For any arbitrary structure considered in this study, the eigenmode coordinate is determined by a projection of the Cartesian displacement vector onto the eigenbasis:

$$u_j = \sum_{\tau\alpha} \xi_\alpha^\tau(j) v_\alpha^\tau. \quad (5)$$

An expansion of the total energy about the reference state is separated into four terms [5]:

$$E(\epsilon_{zz}, u_j; \bar{\eta}) = E_0 + E^{\text{elas}}(\epsilon_{zz}) + E^{\text{disp}}(u_j) + E^{\text{int}}(\epsilon_{zz}, u_j). \quad (6)$$

The misfit strain, $\bar{\eta}$, is a parameter that defines the reference state in the expansion and is not an expansion variable. Thus, E_0 is the energy of the tetragonally relaxed reference structure, and ϵ_{zz} is the out-of-plane strain relative to this reference.

As $\sigma_{zz}, \sigma_{yz}, \sigma_{xz}$, and atomic forces in the reference structures are 0, no first-order terms persist in the expansions. The pure elastic contributions to the total energy are thus described as

$$E^{\text{elas}}(\epsilon_{zz}) = B_2\epsilon_{zz}^2 + B_3\epsilon_{zz}^3 + B_4\epsilon_{zz}^4. \quad (7)$$

For pure displacement terms, second-order cross terms ($u_i u_j$) also cannot persist due to the choice of eigenbasis, and third-order terms vanish due to centrosymmetry of the chosen reference structures under arbitrary homogeneous strain, ensuring that $E(\epsilon_{zz}, v_\alpha^\tau) = E(\epsilon_{zz}, -v_\alpha^\tau)$. The resulting fourth-order expansion for the pure displacement energy contribution is

$$E^{\text{disp}}(u_j) = \sum_j \frac{1}{2}\lambda_j u_j^2 + C_j u_j^4, \quad (8)$$

where j is chosen in this work to include the nine most unstable (or soft) modes. For the interaction terms describing strain-displacement couplings, all second-order terms ($\epsilon_{zz} u_j$) vanish due to centrosymmetry, and the lowest-order term in the expansion, which is the only one retained in the current work, has the form

$$E^{\text{int}}(\epsilon_{zz}, u_j) = \sum_j A_j \epsilon_{zz} u_j^2. \quad (9)$$

It is noted that there is a unique expansion for each composition at each misfit strain, resulting in $3 \times 5 = 15$ sets of expansion coefficients. There are many options for deciding the number of terms to keep in the above expansions. Although $(40 \times 3) - 3 = 117$ different eigenmode degrees of freedom exist, only up to 9 are explicitly included in this work. By considering up to the nine softest eigenmodes, it is ensured that the three ferroelectric modes and the six octahedral rotational modes can always be considered if they are the most unstable. As these modes are commonly observed among perovskite oxides, they are essential in capturing common complex ground-state structures [16]. Further, although the above expansions can be taken to arbitrary order, this work truncates E^{elas} and E^{disp} at fourth order, truncates E^{int} at third order, and does not include cross-coupling displacement mode terms (i.e., $u_i^2 u_j^2$-type terms). These truncations result in the smallest number of terms that still give rise to an expression that is guaranteed to have a bounded minimum. Higher-order terms could be included and would improve the accuracy, but the expansions in the present workflow are used only to find candidate metastable structures for subsequent input into DFT geometry optimizations, and thus the truncation to low order still provides sufficient accuracy for the purposes of this work. Further, the present workflow's use of a distinct energy expansion at each misfit strain greatly helps to reduce the role that higher-order terms play in dictating the local minima of the potential-energy landscape.

Validation of the assumptions underlying this approach are undertaken through comparisons to previous work (see Sec. IV B), and for the compounds considered, the approach is found to be effective in identifying ground-state structures. For other systems requiring a more refined approximation to the energy landscape, the present approach can be extended straightforwardly by including more degrees of freedom and/or including additional higher-order terms.

The expansion coefficients defined in this section are determined through fitting to results of DFT calculations that consider different finite displacements and distortions of the reference structures [5]. Details are discussed in Sec. I of the Supplemental Material [17], which gives an example for the case of $SrTiO_3$. These expansion coefficients correspond to a small subset of those required in the effective Hamiltonian approach presented in Ref. [18], and a significant number of additional fitted parameters would be necessary to study the phase transition behaviors of $SrTiO_3$, $CaTiO_3$, and $SrHfO_3$.

B. Construction of epitaxial phase diagrams

For each of the three compositions, and at each of five misfit strains, a set of candidate structures is generated by analytically solving for all minima of the total energy expansion defined in Sec. II A. These candidate structures are subsequently used as the starting configuration for a DFT calculation in which the structure is relaxed, keeping the in-plane strains fixed at the relevant value of $\bar{\eta}$. After all of the candidate structures have been relaxed, the DFT energies are compared to identify the most energetically stable (i.e., the lowest-energy) state. The result is a set of five low-energy structures, one for each value of the misfit strain ($\bar{\eta} = -2\%, -1\%, 0\%, 1\%$, and 2%). For each of these five structures, an energy–versus–misfit strain curve is generated by re-relaxing the structures, with the in-plane strain fixed at several values of $\bar{\eta}$ on a finer grid spanning values from -4% to 4%. Prior to these structural relaxations, the atom positions are given small random displacements in order to reduce the symmetry to $P1$, guaranteeing that the final structures are stable with respect to distortions of the 40-atom cells. It is emphasized that out-of-plane shear strain degrees of freedom are not constrained during these structural optimizations, and the resulting lattice need not be tetragonal. The lowest-energy phase at each misfit strain comprises the set of ground-state structures based on the 40-atom supercells, and from these structures the zero-temperature phase diagram versus misfit strain is thus produced.

C. Calculation methods

All *ab initio* DFT calculations made use of the Vienna *ab initio* simulation package (VASP) [19–22], version 5.4.1. A conjugate-gradient algorithm was used for all structural relaxations. As the standard VASP software package does

not allow for arbitrary mechanical boundary conditions, the relaxations under fixed in-plane strain made use of a custom modified version of the software in which certain components of the stress tensor are constrained to 0.

Calculations used the Ceperley-Alder form of the local density approximation (LDA) exchange-correlation functional, as parameterized by Perdew and Zunger [23], with the electron-ion interaction described by the projector augmented wave method [24,25]. Force-constant matrices were calculated by density-functional perturbation theory [26] at the zone center for each of the reference $2 \times 2 \times 2$ supercells. For all calculations required to compute expansion coefficients, and for the subsequent relaxations of candidate structures, use was made of a 600-eV plane-wave cutoff energy, $3 \times 3 \times 3$ Monkhorst-Pack sampling of the Brillouin zone [27], and Gaussian smearing of 0.01 eV.

More refined computational parameters were used in the final relaxations and polarization calculations in the construction of the ground-state phase diagrams. In these more refined calculations, an 800-eV plane-wave cutoff energy and a $4 \times 4 \times 4$ Monkhorst-Pack sampling of the Brillouin zone were used. All relaxations of the structures were continued until the forces and out-of-plane stresses converged to magnitudes within 0.001 eV/Å and 0.005 eV/f.u., respectively, where eV/f.u. is per five-atom formula unit. The resulting level of convergence in energy differences is to within 0.1 meV/f.u.

The Berry phase approach, as described in the modern theory of polarization [28], was used to calculate the electric polarization vector at each misfit strain. All calculations assume a fixed (vanishing) external electric field corresponding to thin films surrounded by perfectly charge-compensating electrodes, as discussed in Refs. [29] and [30]. Further, use of the LDA in the present work leads to well-known systematic errors in the calculated lattice constants, amounting to an underestimation of their values of the order of a percent [2,5]. Further discussion of the effect of the exchange-correlation functional is given in the Supplemental Material [17], in which the phase diagram for $CaTiO_3$ is recalculated using the SCAN meta-GGA functional [31]. A comparison between the LDA and the SCAN results suggests that the predicted phases and their order with respect to misfit strain are equivalent, with the phase boundaries of SCAN shifted to epitaxial lattice constants that are approximately 1% larger in magnitude compared to those for the LDA.

III. RESULTS

A. Properties of bulk systems

The ground-state structures of bulk, unstrained $SrTiO_3$, $CaTiO_3$, and $SrHfO_3$ were calculated for use as energetic references, and their properties are listed in Table I. Included in this table is the Goldschmidt tolerance factor [33] t, which is defined as

$$t = \frac{R_{A\text{-O}}}{\sqrt{2} R_{B\text{-O}}}, \tag{10}$$

where $R_{A\text{-O}}$ and $R_{B\text{-O}}$ are the ideal A-O and B-O perovskite structure bond lengths.

$SrTiO_3$ adopts the tetragonal $I4/mcm$ structure, obtained by condensing an out-of-phase rotational instability (R_4^+ in the irreducible representation notation of Ref. [32]) about the direction of elongation. $CaTiO_3$ and $SrHfO_3$ adopt the orthorhombic $Pnma$ structure, obtained by condensing equal amplitudes of the R_4^+ mode about two axes and a unique amplitude of an in-phase rotational instability (M_3^+) about a third axis. Additional A-site displacement modes further contribute to the latter two structures, and these modes are discussed in more detail in the context of epitaxial structures in Sec. IV D. None of the three bulk structures exhibits a macroscopic polarization.

TABLE I. Bulk properties of the three compositions considered, including calculated cubic lattice constants, Goldschmidt tolerance factors [33], and space groups and Glazer systems [16] of the bulk ground-state phase.

Formula	a_0 (Å)	Tolerance factor t	Space group	Glazer system
$SrTiO_3$	3.86	1.001	$I4/mcm$	$a_0^0 a_0^0 c_0^-$
$CaTiO_3$	3.81	0.946	$Pnma$	$a_0^- a_0^- c_0^+$
$SrHfO_3$	4.07	0.949	$Pnma$	$a_0^- a_0^- c_0^+$

B. Eigenmode properties and expansion coefficients

Table II lists the properties of the nine most unstable or softest stable displacement eigenmodes at five misfit strains for $SrTiO_3$, $CaTiO_3$, and $SrHfO_3$. Properties listed include the Glazer system (detailed in Ref. [16]), eigenvalue, and mode polarization vector, $\vec{Z}$, which is defined as the dot product of the Born effective charge tensor [34] of the reference structure with the associated eigenvector:

$$\vec{Z}_i = \sum_{\tau\alpha} \xi_\alpha^\tau(i) Z_\alpha^{*\tau}. \tag{11}$$

This vector represents the macroscopic polarization that develops per small increase in the ith eigenmode coordinate. For plots of the eigenvalues of many of the eigenmodes listed in Table II, see the bottom panels in Fig. 1. Table SI in the Supplemental Material [17] lists the expansion coefficients defined in Sec. II A for five values of the misfit strain for $SrTiO_3$, $CaTiO_3$, and $SrHfO_3$.

C. Epitaxial phase diagrams

Figure 1 plots the energies, polarization components, and eigenmode amplitudes of the epitaxial ground-state structures and the force-constant matrix eigenvalues of the tetragonal reference structures versus misfit strain for $SrTiO_3$, $CaTiO_3$, and $SrHfO_3$. The top panel in each plot corresponds to the energy and polarization of the ground-state structure as a function of the misfit strain. The reference energy for each compound is that of the corresponding bulk, fully relaxed structure listed in Table I. The energy values plotted in Fig. 1 can thus be interpreted as the elastic energy of the epitaxially constrained phase, and the more positive this energy is, the higher the driving force for strain relaxation, e.g., through the formation of misfit dislocations. Misfit strains corresponding to phase transitions are indicated by dashed vertical lines, and the space groups of the epitaxial phases in each misfit strain regime are indicated in the top panels. The horizontal scale

TABLE II. Properties of the nine softest eigen-displacement modes at various misfit strains for $SrTiO_3$, $CaTiO_3$, and $SrHfO_3$. Properties listed include the tilt system of each eigenmode, as denoted by the modified Glazer notation, the eigenvalue, λ_i (eV/Å^2), of the ith displacement mode, and the mode polarization vector, $\vec{Z}_i$ (C/m^2), as defined in Eq. (11) in Sec. III B. An asterisk denotes a trivial translational eigenmode which must have an eigenvalue of 0 and vanishing polarization vector, while N/A denotes a displacement mode that cannot be described by the Glazer notation.

		Eigenmode index								
Misfit strain		1	2	3	4	5	6	7	8	9
$SrTiO_3$										
	Glazer	$a_0^0a_0^0c_+^0$	$a_0^0a_0^0c_0^-$	$a_0^0a_0^0c_0^+$	$a_0^-b_0^0b_0^0$	$a_0^0b_0^-a_0^0$				$a_0^+b_0^0b_0^0$
−2%	λ_i	−2.06	−1.1	−0.69	−0.46	−0.46	*	*	*	0.07
	$\vec{Z}_i$	(0 0 0.9)	**0**	**0**	**0**	**0**				**0**
	Glazer	$a_0^0a_0^0c_+^0$	$a_0^0a_0^0c_0^-$	$a_0^-b_0^0b_0^0$	$a_0^0b_0^-a_0^0$	$a_0^0a_0^0c_0^+$	$a_0^+b_0^0b_0^0$	$a_0^0b_0^+a_0^0$		
−1%	λ_i	−0.81	−0.76	−0.49	−0.49	−0.33	−0.01	−0.01	*	*
	$\vec{Z}_i$	(0 0 0.9)	**0**	**0**	**0**	**0**	**0**	**0**		
	Glazer	$a_0^-b_0^0b_0^0$	$a_0^0b_0^-a_0^0$	$a_0^0a_0^0c_0^-$	$a_0^+b_0^0b_0^0$	$a_0^0b_0^+a_0^0$	$a_0^0a_0^0c_0^+$			
0%	λ_i	−0.49	−0.49	−0.48	−0.05	−0.05	−0.04	*	*	*
	$\vec{Z}_i$	**0**	**0**	**0**	**0**	**0**	**0**			
	Glazer	$a_+^0b_0^0b_0^0$	$a_0^0b_+^0a_0^0$	$a_0^-b_0^0b_0^0$	$a_0^0b_0^-a_0^0$	$a_0^0a_0^0c_0^-$	$a_0^+b_0^0b_0^0$	$a_0^0b_0^+a_0^0$		
1%	λ_i	−1.18	−1.18	−0.52	−0.52	−0.27	−0.12	−0.12	*	*
	$\vec{Z}_i$	(0.9 0 0)	(0 0.9 0)	**0**	**0**	**0**	**0**	**0**		
	Glazer	$a_+^0b_0^0b_0^0$	$a_0^0b_+^0a_0^0$	N/A	N/A	$a_0^-b_0^0b_0^0$	$a_0^0b_0^-a_0^0$	$a_0^+b_0^0b_0^0$	$a_0^0b_0^+a_0^0$	$a_0^0a_0^0c_0^-$
2%	λ_i	−2.81	−2.81	−1.4	−1.4	−0.52	−0.52	−0.14	−0.14	−0.11
	$\vec{Z}_i$	(0.9 0 0)	(0 0.9 0)	**0**	**0**	**0**	**0**	**0**	**0**	**0**
$CaTiO_3$										
	Glazer	$a_0^0a_0^0c_0^-$	$a_0^0a_0^0c_+^0$	$a_0^0a_0^0c_0^+$	$a_0^-b_0^0b_0^0$	$a_0^0b_0^-a_0^0$	$a_0^+b_0^0b_0^0$	$a_0^0b_0^+a_0^0$	$a_+^0b_0^0b_0^0$	$a_0^0b_+^0a_0^0$
−2%	λ_i	−3.53	−3.27	−3.23	−3.05	−3.05	−2.69	−2.69	−1.2	−1.2
	$\vec{Z}_i$	**0**	(0 0 0.8)	**0**	**0**	**0**	**0**	**0**	(0.67 0 0)	(0 0.67 0)
	Glazer	$a_0^0a_0^0c_0^-$	$a_0^-b_0^0b_0^0$	$a_0^0b_0^-a_0^0$	$a_0^0a_0^0c_0^+$	$a_0^+b_0^0b_0^0$	$a_0^0b_0^+a_0^0$	$a_0^0a_0^0c_+^0$	$a_+^0b_0^0b_0^0$	$a_0^0b_+^0a_0^0$
−1%	λ_i	−3.15	−2.94	−2.94	−2.84	−2.61	−2.61	−2.35	−1.47	−1.47
	$\vec{Z}_i$	**0**	**0**	**0**	**0**	**0**	**0**	(0 0 0.76)	(0.69 0 0)	(0 0.69 0)
	Glazer	$a_0^-b_0^0b_0^0$	$a_0^0b_0^-a_0^0$	$a_0^0a_0^0c_0^-$	$a_0^+b_0^0b_0^0$	$a_0^0b_0^+a_0^0$	$a_0^0a_0^0c_0^+$	$a_+^0b_0^0b_0^0$	$a_0^0b_+^0a_0^0$	$a_0^0a_0^0c_+^0$
0%	λ_i	−2.83	−2.83	−2.8	−2.53	−2.53	−2.5	−1.91	−1.91	−1.77
	$\vec{Z}_i$	**0**	**0**	**0**	**0**	**0**	**0**	(0.72 0 0)	(0 0.72 0)	(0 0 0.71)
	Glazer	$a_0^-b_0^0b_0^0$	$a_0^0b_0^-a_0^0$	$a_0^0a_0^0c_0^-$	$a_+^0b_0^0b_0^0$	$a_0^0b_+^0a_0^0$	$a_0^+b_0^0b_0^0$	$a_0^0b_0^+a_0^0$	$a_0^0a_0^0c_0^+$	$a_0^0a_0^0c_+^0$
1%	λ_i	−2.73	−2.73	−2.53	−2.5	−2.5	−2.45	−2.45	−2.22	−1.4
	$\vec{Z}_i$	**0**	**0**	**0**	(0.75 0 0)	(0 0.75 0)	**0**	**0**	**0**	(0 0 0.66)
	Glazer	$a_+^0b_0^0b_0^0$	$a_0^0b_+^0a_0^0$	$a_0^-b_0^0b_0^0$	$a_0^0b_0^-a_0^0$	$a_0^+b_0^0b_0^0$	$a_0^0b_0^+a_0^0$	$a_0^0a_0^0c_0^-$	$a_0^0a_0^0c_0^+$	$a_0^0a_0^0c_+^0$
2%	λ_i	−3.24	−3.24	−2.61	−2.61	−2.35	−2.35	−2.29	−1.98	−1.21
	$\vec{Z}_i$	(0.78 0 0)	(0 0.78 0)	**0**	**0**	**0**	**0**	**0**	**0**	(0 0 0.61)
$SrHfO_3$										
	Glazer	$a_0^0a_0^0c_0^-$	$a_0^0a_0^0c_0^+$	$a_0^-b_0^0b_0^0$	$a_0^0b_0^-a_0^0$	$a_0^+b_0^0b_0^0$	$a_0^0b_0^+a_0^0$	$a_0^0a_0^0c_+^0$	N/A	N/A
−2%	λ_i	−2.74	−2.46	−2.27	−2.27	−1.91	−1.91	−1.31	−0.48	−0.45
	$\vec{Z}_i$	**0**	**0**	**0**	**0**	**0**	**0**	(0 0 -0.45)	**0**	**0**
	Glazer	$a_0^0a_0^0c_0^-$	$a_0^-b_0^0b_0^0$	$a_0^0b_0^-a_0^0$	$a_0^0a_0^0c_0^+$	$a_0^+b_0^0b_0^0$	$a_0^0b_0^+a_0^0$	$a_0^0a_0^0c_+^0$	$a_+^0b_0^0b_0^0$	$a_0^0b_+^0a_0^0$
−1%	λ_i	−2.33	−2.11	−2.11	−2.04	−1.8	−1.8	−0.72	−0.21	−0.21
	$\vec{Z}_i$	**0**	**0**	**0**	**0**	**0**	**0**	(0 0 -0.42)	(0.38 0 0)	(0 0.38 0)
	Glazer	$a_0^-b_0^0b_0^0$	$a_0^0b_0^-a_0^0$	$a_0^0a_0^0c_0^-$	$a_0^+b_0^0b_0^0$	$a_0^0b_0^+a_0^0$	$a_0^0a_0^0c_0^+$	$a_+^0b_0^0b_0^0$	$a_0^0b_+^0a_0^0$	$a_0^0a_0^0c_+^0$
0%	λ_i	−1.98	−1.98	−1.97	−1.69	−1.69	−1.68	−0.41	−0.41	−0.39
	$\vec{Z}_i$	**0**	**0**	**0**	**0**	**0**	**0**	(0.39 0 0)	(0 0.39 0)	(0 0 0.39)
	Glazer	$a_0^-b_0^0b_0^0$	$a_0^0b_0^-a_0^0$	$a_0^0a_0^0c_0^-$	$a_0^+b_0^0b_0^0$	$a_0^0b_0^+a_0^0$	$a_0^0a_0^0c_0^+$	$a_+^0b_0^0b_0^0$	$a_0^0b_+^0a_0^0$	N/A
1%	λ_i	−1.88	−1.88	−1.67	−1.61	−1.61	−1.38	−0.74	−0.74	−0.41
	$\vec{Z}_i$	**0**	**0**	**0**	**0**	**0**	**0**	(0.39 0 0)	(0 0.39 0)	**0**
	Glazer	$a_0^-b_0^0b_0^0$	$a_0^0b_0^-a_0^0$	$a_0^+b_0^0b_0^0$	$a_0^0b_0^+a_0^0$	$a_0^0a_0^0c_0^-$	$a_0^0a_0^0c_0^+$	$a_+^0b_0^0b_0^0$	$a_0^0b_+^0a_0^0$	N/A
2%	λ_i	−1.78	−1.78	−1.53	−1.53	−1.41	−1.12	−1.11	−1.11	−0.77
	$\vec{Z}_i$	**0**	**0**	**0**	**0**	**0**	**0**	(0.39 0 0)	(0 0.39 0)	**0**

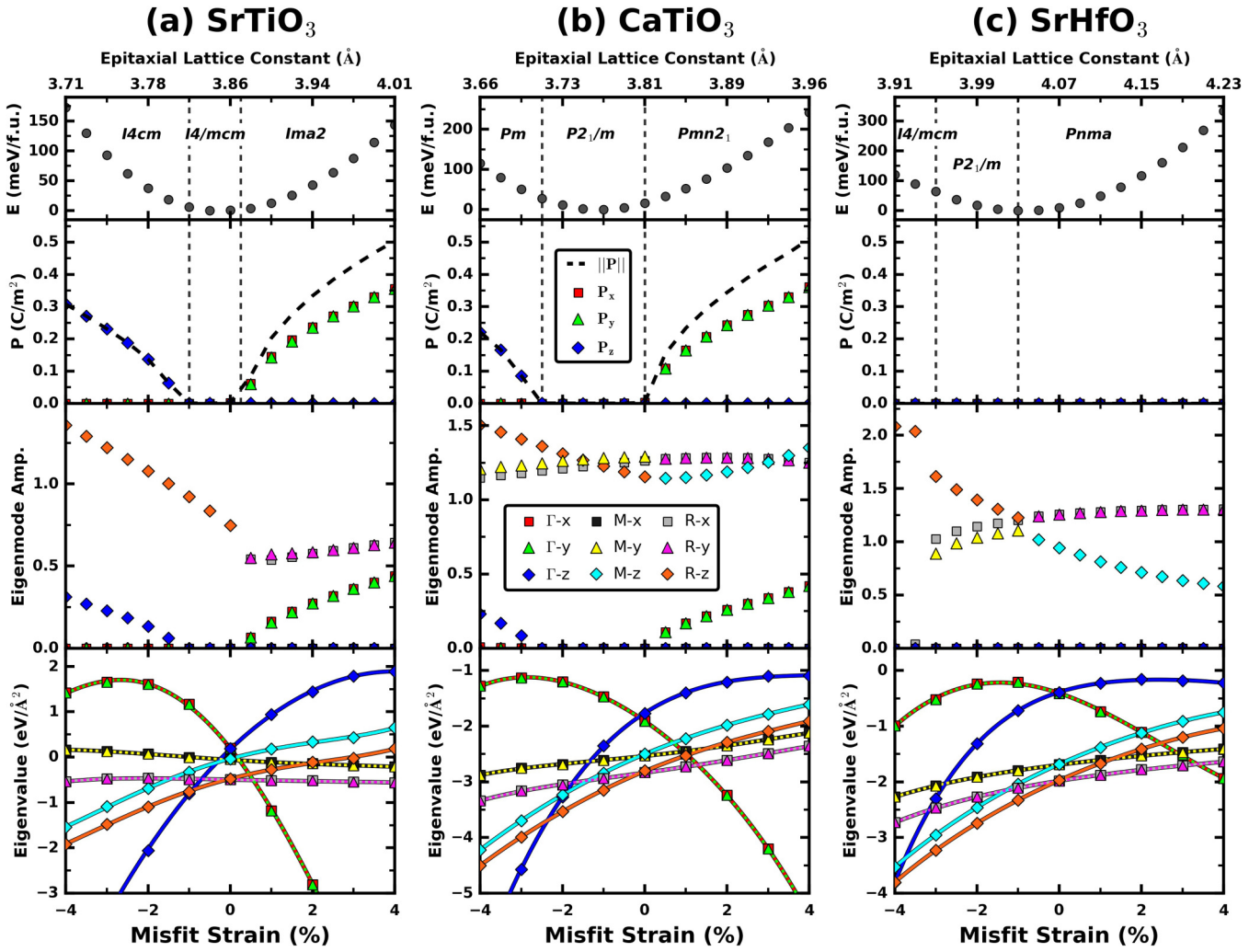

FIG. 1. Plots of ground-state epitaxial structure energies, polarization components, eigenmode amplitudes, and tetragonal reference structure eigenvalues versus misfit strain for (a) $SrTiO_3$, (b) $CaTiO_3$, and (c) $SrHfO_3$. Absolute values of polarization components are taken for visualization purposes. The in-plane lattice constant of the epitaxial structure at each misfit strain is indicated on the top axis. The lower legend corresponds to the eigenmodes shown in Fig. 2 realized down the x, y, or z axis.

given at the top of each figure indicates the cubic substrate lattice constant, a, required to produce the given degree of misfit strain, with $a = a_0(\bar{\eta} + 1)$.

The eigenmode amplitudes shown in the middle panels are determined by Eq. (5). These measure the degree to which the three FE eigenmodes at Γ [Fig. 2(a)] and six rotational displacement eigenmodes at the M [Fig. 2(b)] and R [Fig. 2(c)] boundary points of the Brillouin zone of the cubic perovskite compound have condensed in the ground-state epitaxial structures. The eigenvalues corresponding to these nine modes are plotted in the bottom panels and are determined from diagonalization of the force-constant matrices of the tetragonal reference structures.

Figure 1(a) plots the ground-state epitaxial properties for $SrTiO_3$. Under strong biaxial compression, a polar $I4cm$ phase is predicted having two displacement modes activated, an out-of-plane octahedral rotation R_4^+ mode (orange diamonds in the middle and bottom panels), and an out-of-plane zone-centered FE mode (blue diamonds). These are also the two most unstable modes of the reference tetragonal structures in the compressive regime, as indicated in the bottom panel. As the strain becomes less compressive, both modes gradually diminish until the FE mode entirely vanishes, giving way to the paraelectric $I4/mcm$ phase beginning at -1% misfit strain. In this region, only the R_4^+ mode persists, and its amplitude continues to diminish until 0.25% misfit strain, at which point the polar $Ima2$ phase sets in through a first-order transition. The $Ima2$ phase consists of four active displacement modes, including two in-plane octahedral rotation R_4^+ modes (gray squares and purple triangles) and two in-plane zone-centered FE modes (red squares and green triangles). These are also the four most unstable modes of the reference tetragonal structures in the tensile strain regime, as shown in the bottom panel. With increasing tensile strain, the two in-plane octahedral rotation R_4^+ modes in the $Ima2$ phase tend to remain approximately constant in their eigenmode amplitudes, while the in-plane FE modes gradually increase in eigenmode amplitude. The elastic energy curve for $SrTiO_3$ is symmetric with respect to misfit

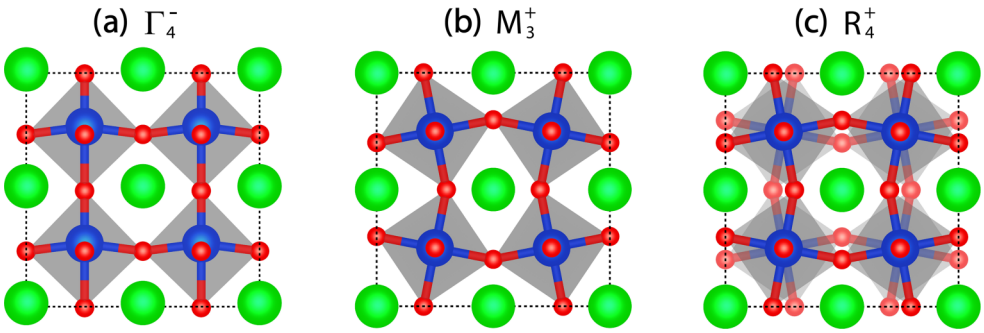

FIG. 2. The three most dominant unstable eigenmodes for epitaxial $SrTiO_3$, $CaTiO_3$, and $SrHfO_3$. (a) The zone-centered FE mode, often transforming like the irrep Γ_4^-; (b) the in-phase AFD octahedral rotation, transforming like the irrep M_3^+; and (c) the out-of-phase AFD octahedral rotation, transforming like the irrep R_4^+. All three can be independently realized down each of the three unit-cell axes. This figure was created using VESTA [35].

strain, having a minimum at 0% misfit strain and approximately 150 meV/f.u. of elastic energy at the extremes of compressive and tensile misfit strain considered.

Figure 1(b) plots the ground-state epitaxial properties for $CaTiO_3$. Compared to $SrTiO_3$, the predicted phases of $CaTiO_3$ involve a more complicated interplay of a larger number of displacement modes. From -4% to -2.5% misfit strain, the polar Pm phase is predicted as a ground-state structure, for which the atomic displacements involve a combination of an out-of-plane FE, in-plane R_4^+ rotation, in-plane M_3^+ rotation, and out-of-plane R_4^+ rotation mode. As the magnitude of the biaxial compressive strain is reduced, the two in-plane rotational modes slightly increase in amplitude, while the two out-of-plane modes diminish. At -2.5% misfit strain, the amplitude of the out-of-plane FE mode vanishes, and the nonpolar $P2_1/m$ parent phase becomes stable in a smooth second-order transition. This phase persists from -2.5% to 0% misfit strain, over which the in-plane rotation modes continue to slowly increase in amplitude while the out-of-plane rotation mode continues to diminish. At zero misfit strain, the three octahedral modes are discontinuously replaced by two in-plane FEs, one out-of-plane M_3^+ rotation, and two in-plane R_4^+ rotation modes in a first-order transition to the polar $Pmn2_1$ phase. This phase persists to the extreme of tensile strain considered, with the in-plane FE modes gradually increasing and the octahedral modes remaining roughly constant in amplitude. The elastic energy curve of $CaTiO_3$ has its minimum shifted to -1% misfit strain. This shift is possible because the energy curve is referenced to the fully relaxed bulk $CaTiO_3$ structure, while the misfit strain is referenced to the equilibrium lattice constant of a bulk cubic structure. The energy curve reflects this with 100 meV/f.u. of elastic energy at -4% misfit strain and 250 meV/f.u. at 4% misfit strain.

Figure 1(c) plots the calculated properties for $SrHfO_3$. Like $CaTiO_3$, this system exhibits a complicated interplay of many displacement modes. Under a large compressive strain, a paraelectric $I4/mcm$ phase is predicted, having only an out-of-plane R_4^+ rotation mode active. At -3% misfit strain, there is a first-order transition to a paraelectric $P2_1/m$ phase. Continuing to -1% misfit strain, there is another first-order phase transition to a paraelectric $Pnma$ phase that is like the bulk $Pnma$ phase, but with a tetragonal lattice instead of an orthorhombic one. An orthorhombic rather than a tetragonal space group is adopted in this case due to symmetry-lowering atomic displacements in the epitaxial ground-state structure. This $Pnma$ phase remains stable to the extreme of tensile strain considered, with the in-plane R_4^+ rotation mode amplitudes remaining nearly constant, and the out-of-plane M_3^+ mode amplitude diminishing. The elastic energy curve for $SrHfO_3$ is asymmetric, having a -1% shift in the minimum, 100 meV/f.u. elastic energy at -4% misfit strain, and over 300 meV/f.u. elastic energy at 4% misfit strain.

IV. DISCUSSION

A. Comparison to previous calculations

In order to validate the accuracy of the present computational approach, results are compared in this section to previous DFT calculations that include some form of input from experimental observations or phenomenological theory. As discussed below, the present work correctly leads to the identification of stable phases reported previously for epitaxially strained $SrTiO_3$ and $CaTiO_3$. Quantitative discrepancies with these previous computational investigations, which do not relate to the efficacy of the present structure optimization approach, are found and attributed to differences in the numerical parameters in the underlying DFT calculations.

Lin *et al.* [14] use DFT to calculate the epitaxial phase diagram of $SrTiO_3$ by considering all phases predicted by phenomenological Landau theory [36]. The general polarization behavior and stable phases at the extremes of misfit strain compare very well to those in the present work. Specifically, the results of both studies feature the stability of an $I4cm$ phase with enhanced out-of-plane polarization under compression and an $Ima2$ phase with enhanced in-plane polarization under tension. Near 0% misfit strain, the two works differ in their predicted phases. While the present work predicts a paraelectric $I4/mcm$ phase near 0% misfit strain, Ref. [14] predicts a total of three phases in this same region of strains, including, in addition to the $I4/mcm$ phase, two other polar phases with $Ima2$ and $Fmm2$ symmetries. These differences arise due to the near energetic degeneracy of the competing phases, such that differences in the parameters underlying the DFT calculations can influence conclusions about relative stability. To ensure this is the case, rather than being due to the underlying structural optimization procedure of the

present workflow, the energies of the $Ima2$ and $Fmm2$ phases were computed using the computational parameters given in Sec. II C, featuring a plane-wave cutoff nearly twice as large as that employed in Ref. [14]. Consistent with the results shown in Fig. 1, with the DFT parameters employed in the present work, it was verified that the lowest-energy structure was the one with $I4/mcm$ symmetry, with the $Ima2$ and $Fmm2$ polymorphs being higher in energy and therefore metastable.

For $CaTiO_3$, Eklund *et al.* [13] computed epitaxial phase diagrams using DFT by considering the relative stability of a number of candidate phases derived from the experimentally observed bulk phase. There is good agreement between the present results and the work in Ref. [13] in terms of the stable phases predicted, with both studies determining the $P2_1/m$ phase to be stable under moderate compression and the $Pmn2_1$ phase to be stable under tension. The strain corresponding to the transition between these two phases is quantitatively different in the two studies, however: Eklund *et al.* find a value of $\bar{\eta} = 0\%$, while in the present work this value is approximately 2%. As above, these quantitative differences are likely a consequence of the different DFT parameters employed in the two studies.

B. The role of non-zone-center displacement modes

In previous work by the authors [7], epitaxial phase diagrams were calculated using an approach similar to that described here but disallowing relaxations associated with non-zone-center displacement modes. In other words, the work in Ref. [7] considered only phases that could be derived from the perovskite structure through homogeneous strains and zone-centered FE displacement modes. A comparison of the results obtained in Ref. [7] with those obtained in the present work is therefore of interest, as it highlights the role of non-zone-centered distortions, such as octahedral rotations, in determining the structural, energetic, and polarization dependences on epitaxial strain. This information is of interest because non-zone-centered distortions may be frozen out in very thin films if they increase the interfacial energy, while they may be present in thicker films if they reduce the strain energy.

For $SrTiO_3$, the effect of non-zone-centered distortions is to widen the range of stability of the paraelectric phase by nearly 0.5% misfit strain. Specifically, octahedral rotations reduce the strain energy by 147 meV/f.u. at -4% misfit strain, and by 86 meV/f.u. at 4% misfit strain. This implies that rotational modes reduce the elastic energy and should allow for larger critical thicknesses for epitaxial growth. Under compressive epitaxial strain, the out-of-plane polarization is nearly halved when the out-of-plane rotation is allowed, implying an unfavorable coupling with the out-of-plane FE mode. In contrast, under tensile misfit strain, the presence of the two in-plane R_4^+ octahedral rotation modes does not significantly change the polarization compared to the results obtained from disallowing non-zone-center distortions.

For $SrHfO_3$, much larger effects of non-zone-center modes are found. The elastic energy is reduced by 343 meV/f.u. at -4% misfit strain and 109 meV/f.u. at 4% misfit strain when the non-zone-centered modes are allowed. Also, in the calculations where non-zone-center distortions are disallowed, large polarizations are computed, up to 0.56 C/m^2, and a direct transition from a $P4mm$ phase with purely out-of-plane polarization to a $Pmm2$ phase with purely in-plane polarization is predicted around 0% misfit strain. The presence of non-zone-centered distortions in $SrHfO_3$ strongly suppresses these two phenomena, giving way to a paraelectric film over the entire range of epitaxial strain between -4% and 4%.

C. Predominant displacement modes

The atomic displacements calculated in the present work for the epitaxial ground-state structures of $SrTiO_3$, $CaTiO_3$, and $SrHfO_3$ can be predominantly decomposed into a small set of displacement eigenmodes. Figure 2 shows the displacement patterns of the most dominant unstable eigenmodes, including a zone-centered FE distortion wherein the B cations shift against the other sublattices [Fig. 2(a); irreducible representation Γ_4^-] and two types of AFD octahedral rotations wherein the oxygen octahedra rotate either out of phase [Fig. 2(b); R_4^+] or in phase [Fig. 2(c); M_3^+] along an axis. Note that the irreducible representation of the FE mode can vary with the composition and misfit strain and need not be Γ_4^-, although this is the most common, whereas the octahedral rotation modes are uniquely determined by symmetry. Each of these three displacement patterns can be independently realized along each of the three orthogonal unit cell axes, leading to nine dominating displacement eigenmodes. Linear combinations of these nine eigenmodes account for 95.8% of the total atomic displacement predicted in the ground-state epitaxial phases of $SrTiO_3$, 70.1% of the total displacement in $CaTiO_3$, and 77.2% in $SrHfO_3$.

Even in cases where other displacement modes are more unstable in the reference tetragonal structures, combinations of the nine modes described in the previous paragraph still dominate in their contribution to the atomic displacements of the relaxed epitaxial ground-state structures. Table II lists the sets of nine eigenmodes with the most unstable eigenvalues for each of the reference tetragonal structures at various misfit strains. In some cases, denoted "N/A" in the Glazer system entry in Table II, these sets include modes other than the nine dominant modes described in the previous paragraph. However, even when these other modes are more unstable, the nine modes described in the previous paragraph still dominate in contributions to calculated displacement patterns in the relaxed ground-state structures. This tendency implies that the displacement modes illustrated in Sec. IV C have a more optimal balance of strong instability and favorable coupling with each other than other subsets of displacement modes.

For example, when $\bar{\eta} \geqslant 2\%$ for $SrTiO_3$, two symmetry-equivalent in-plane AFD modes have more negative eigenvalues in the reference tetragonal structures than all six of the R_4^+ and M_3^+ rotational modes. Yet these two in-plane AFD modes do not contribute significantly to the calculated displacements in the relaxed ground-state structures of $SrTiO_3$ for strains ranging between 2% and 4%, while three of the six R_4^+ and M_3^+ rotational modes make large contributions to these displacements. Likewise, under large biaxial compressive or tensile strains, $SrHfO_3$ also has other unstable eigenmodes in the tetragonal reference structures that ultimately do not

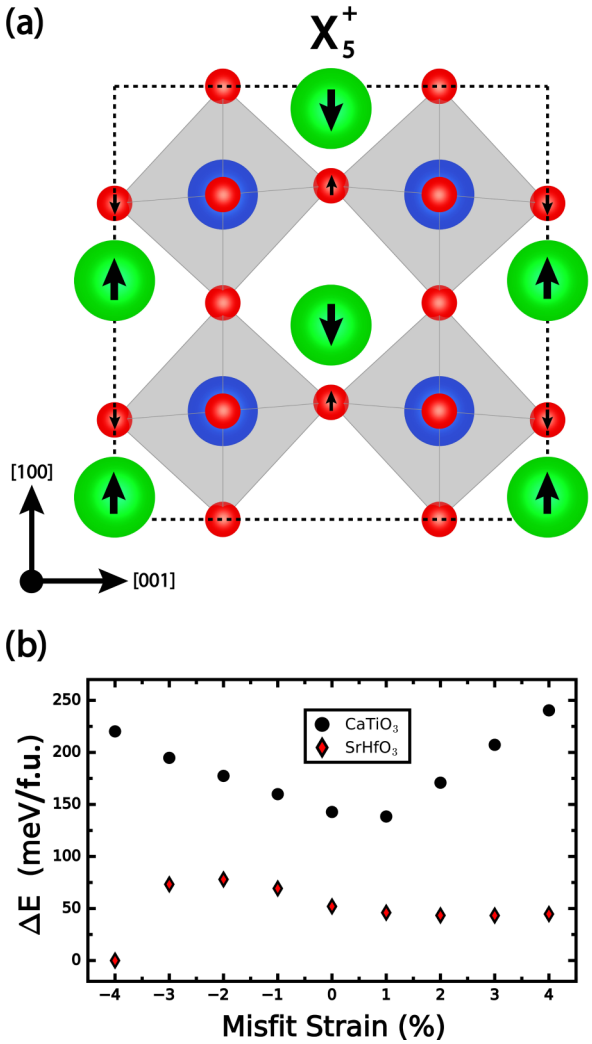

FIG. 3. (a) Antipolar *A*-site displacement mode (irreducible representation X_5^+). This mode can be independently realized down each of the three unit-cell axes. (b) Metastability relative to the ground-state structures of $CaTiO_3$ and $SrHfO_3$ resulting from the eigenmode amplitudes of all modes other than the nine mentioned in Sec. IV C being set to 0. Panel (a) was created using VESTA [35].

contribute significantly to the atomic displacements in the relaxed ground-state structures.

D. Role of *A*-site bonding

Although the nine dominant displacement modes illustrated in Fig. 2 largely describe the atomic displacements calculated for $SrTiO_3$, the ground-state epitaxial structures of $CaTiO_3$ and $SrHfO_3$ also have nonnegligible atomic displacement contributions from a few additional stable or weakly unstable displacement eigenmodes. Of these, the most relevant is an antipolar *A*-site mode transforming like the irreducible representation X_5^+, shown in Fig. 3(a). As described in detail in Ref. [6], the X_5^+ mode is energetically favorable when both the R_4^+ and the M_3^+ rotational modes are present. Thus, most epitaxial ground-state structures for $CaTiO_3$ and $SrHfO_3$ predicted in this work show a significant antipolar shift in the *A* sublattice with some dependence on misfit strain. Although these modes contribute less than 30% of the total atomic displacement in the relaxed structures, their impact on the energy is still significant.

In order to determine the energetic influence of these eigenmodes having predominantly *A*-site displacements, the energies of the ground-state structures for $CaTiO_3$ and $SrHfO_3$ are recalculated for modified structures in which only the contributions to the displacements associated with the nine dominant eigenmodes illustrated in Fig. 2 are kept, all other amplitudes being set to 0. The primary effect of this constraint is to disallow the structure to shift the *A*-site sublattices. Figure 3(b) shows the resulting energy curves versus misfit strain for $CaTiO_3$ and $SrHfO_3$. For $CaTiO_3$, removing all but the nine dominant modes from the structures increases the energy by up to 250 meV/f.u., with the most pronounced effects at the extremes of misfit strain. For $SrHfO_3$, the energetic influence is smaller, but still significant, with a maximum increase in energy of 80 meV/f.u at $\bar{\eta} = -2\%$. At $\bar{\eta} = -4\%$, contributions of modes other than the dominant nine vanish in $SrHfO_3$.

The reason these *A*-site displacement modes are important in $CaTiO_3$ and $SrHfO_3$, but not in $SrTiO_3$, can be explained by simple geometrical considerations. The relative ratios of the *A*- and *B*-cation radii, as characterized by the Goldschmidt tolerance factor (t) [33], are very different in these two cases. While $SrTiO_3$ ($t = 1.001$) has a tolerance factor that is close to unity, implying that the *A* and *B* cations have radii nearly perfectly suited to the ideal perovskite structure, $CaTiO_3$ ($t = 0.946$) and $SrHfO_3$ ($t = 0.949$) have *A* cations that are relatively too small. As a result, the *A*-site coordination environment is unfavorable in the latter two systems, which explains why the eigenvalues of the $CaTiO_3$ and $SrHfO_3$ tetragonal reference structures are consistently 2–3 eV/Å^2 lower in value than those of $SrTiO_3$ for both the FE and the AFD rotational eigenmodes (see bottom panels in Fig. 1). Both the FE and the AFD eigenmodes can optimize the *A*-site bonding, although octahedral rotations tend to do so more effectively and, thus, contribute more significantly to atomic displacements in the ground-state structures of $CaTiO_3$ and $SrHfO_3$ [6]. These rotations alone, however, are not enough to satisfy the *A*-site bonding preferences, which is why additional displacement modes, such as the antipolar *A*-site X_5^+ eigenmode shown in Fig. 3(a), also condense in the structure. These modes further serve to minimize *A*-O repulsion and optimize the undersized *A*-site's coordination [6]. This can be visualized in the displacement pattern of the X_5^+ mode, which brings the *A* cations closer to the square oxygen interstice, while also drawing some of the equatorial oxygen atoms toward the *A* cations. Figure 3(b) illustrates that these *A*-site bond-optimizing modes can be important in lowering the strain energy and that the degree to which these modes are needed to optimize the *A*-site bonding are highly sensitive to both the misfit strain and the composition of the system.

E. Behavioral trends

Irrespective of differences in cation bonding preferences between $SrTiO_3$, $CaTiO_3$, and $SrHfO_3$, the results of this work demonstrate many shared features among the behavior of the three compositions under epitaxy. In all three systems, application of misfit strain consistently destabilizes the *B*-site

coordination environment, leading to increasing FE eigenmode instabilities under both compression and tension. Increasing biaxial compressive strains lead to the out-of-plane FE displacement mode becoming more unstable, while increasing biaxial tensile strains always leads to the two in-plane FE modes becoming more unstable. The bottom panels in Fig. 1 indicate for all three systems that the FE modes of the tetragonal reference structures couple much more strongly to misfit strain than any of the octahedral rotation modes. The next strongest couplings occur in the two out-of-plane rotation modes, which are both strongly destabilized by increasing compressive strains, while the in-plane rotation modes have the weakest coupling to misfit strain.

V. SUMMARY AND CONCLUSIONS

Presented in this work is a computational framework for the calculation of ground-state epitaxial phase diagrams of ferroelectric perovskite oxides. This framework employs expansions of the total energy at various misfit strains with respect to soft-mode displacements and homogeneous deformations, in order to locate candidate ground-state structures, which are then further optimized through DFT calculations. Competing phases are predicted entirely from first principles, with no assumptions made regarding which set of displacement modes to consider and no requirement of input information from experimental measurements. This method also considers the important effects of AFD and *A*-site displacement modes in ground-state epitaxial phases. The approach outlined in this work for identifying ground-state phases under epitaxial strain can be used in future work to treat a larger range of perovskite systems in order to explore compositional trends more broadly. This approach is demonstrated in the present work in an application to three perovskite oxides, $SrTiO_3$, $CaTiO_3$, and $SrHfO_3$, over a range of epitaxial strains applied parallel to the (001) plane. The main conclusions can be summarized as follows.

Compared to calculations in which relaxations associated with non-zone-centered displacement modes are disallowed, the present results show that the inclusion of non-zone-centered displacement modes significantly affects the dependence of energy and polarization on misfit strain. Namely, AFD octahedral rotations and associated *A*-site displacement modes tend to strongly suppress polarization and also reduce the epitaxial strain energy. This information has important consequences for the stability of competing phases as a function of the film thickness. Non-zone-centered distortions can be frozen out in very thin films if they increase the interfacial energy with the underlying substrate lattice, while these distortions are likely to appear in thicker films because they reduce the strain energy. In this way, competing phases with very different polar properties have the potential to be accessed as a function of the film thickness.

A set of nine displacement modes, three zone-centered FE distortions often transforming like Γ_4^- and six AFD octahedral rotations, three transforming like R_4^+ and three like M_3^+, comprise the largest contributors to the atomic displacements found in the calculated ground-state structures across all of the compositions and misfit strains considered. Combinations of these modes dominate atomic displacements in stable epitaxial phases even when other modes show more unstable eigenvalues in the high-symmetry reference structures. While the atomic displacements of $SrTiO_3$ can almost entirely be decomposed into contributions from these nine dominant displacement modes, those obtained for $CaTiO_3$ and $SrHfO_3$ also contain significant contributions from additional predominantly *A*-site displacement modes. This difference between $SrTiO_3$ and the other two compounds is driven by *A*-site bonding preference. The main effect of these additional modes is an antipolar *A*-site shift that significantly lowers the strain energies of the epitaxial phases by optimizing the coordination geometry of the *A*-site cation.

ACKNOWLEDGMENTS

The authors thank Professor Lane W. Martin for helpful discussions. This work was supported by the U.S. Department of Energy, Office of Science, Office of Basic Energy Sciences, Materials Sciences and Engineering Division, under Contract No. DE-AC02-05-CH11231: Materials Project program KC23MP. T.A. acknowledges a fellowship through the National Science Foundation Graduate Research Fellowship Program (Grant No. DGE1106400).

[1] J. F. Scott, Science **315**, 954 (2007).
[2] M. Dawber, K. M. Rabe, and J. F. Scott, Rev. Mod. Phys. **77**, 1083 (2005).
[3] A. R. Damodaran, J. C. Agar, S. Pandya, Z. Chen, L. Dedon, R. Xu, B. Apgar, S. Saremi, and L. W. Martin, J. Phys. Condens. Matter **28**, 263001 (2016).
[4] R. D. King-Smith and D. Vanderbilt, Phys. Rev. B **49**, 5828 (1994).
[5] O. Diéguez, K. M. Rabe, and D. Vanderbilt, Phys. Rev. B **72**, 144101 (2005).
[6] N. A. Benedek and C. J. Fennie, J. Phys. Chem. C **117**, 13339 (2013).
[7] T. Angsten, L. W. Martin, and M. Asta, Phys. Rev. B **95**, 174110 (2017).
[8] O. Diéguez, S. Tinte, A. Antons, C. Bungaro, J. B. Neaton, K. M. Rabe, and D. Vanderbilt, Phys. Rev. B **69**, 212101 (2004).
[9] J. B. Neaton, C. L. Hsueh, and K. M. Rabe, in *MRS Proceedings*, edited by K. Poeppelmeier, A. Navrotsky, and R. Wentzcovitch (Materials Research Society, Warrendale, PA, 2002), Vol. 718, pp. 311–316.
[10] A. Antons, J. B. Neaton, K. M. Rabe, and D. Vanderbilt, Phys. Rev. B **71**, 024102 (2005).
[11] K. M. Rabe, Curr. Opin. Solid State Mater. Sci. **9**, 122 (2005).
[12] O. Diéguez and D. Vanderbilt, Phase Transit. **81**, 607 (2008).
[13] C. J. Eklund, C. J. Fennie, and K. M. Rabe, Phys. Rev. B **79**, 220101 (2009).
[14] C.-H. Lin, C.-M. Huang, and G. Y. Guo, J. Appl. Phys. **100**, 084104 (2006).

[15] M. de Jong, W. Chen, H. Geerlings, M. Asta, and K. A. Persson, Sci. Data **2**, 150053 (2015).
[16] H. T. Stokes, E. H. Kisi, D. M. Hatch, and C. J. Howard, Acta Crystallogr. **B58**, 934 (2002).
[17] For details on the expansion coefficients, see the Supplemental Material at http://link.aps.org/supplemental/10.1103/PhysRevB.97.134103.
[18] U. V. Waghmare and K. M. Rabe, Phys. Rev. B **55**, 6161 (1997).
[19] G. Kresse and J. Hafner, Phys. Rev. B **47**, 558 (1993).
[20] G. Kresse and J. Hafner, Phys. Rev. B **49**, 14251 (1994).
[21] G. Kresse and J. Furthmüller, Phys. Rev. B **54**, 11169 (1996).
[22] G. Kresse and J. Furthmüller, Comput. Mater. Sci. **6**, 15 (1996).
[23] J. P. Perdew and A. Zunger, Phys. Rev. B **23**, 5048 (1981).
[24] P. E. Blöchl, Phys. Rev. B **50**, 17953 (1994).
[25] G. Kresse and D. Joubert, Phys. Rev. B **59**, 1758 (1999).
[26] S. Baroni, S. De Gironcoli, A. Dal Corso, and P. Giannozzi, Rev. Mod. Phys. **73**, 515 (2001).
[27] H. Monkhorst and J. Pack, Phys. Rev. B **13**, 5188 (1976).
[28] R. Resta and D. Vanderbilt, Top. Appl. Phys. **105**, 31 (2007).
[29] A. M. Kolpak, N. Sai, and A. M. Rappe, Phys. Rev. B **74**, 054112 (2006).
[30] K. M. Indlekofer and H. Kohlstedt, Europhys. Lett. **72**, 282 (2005).
[31] Y. Zhang, J. Sun, J. P. Perdew, and X. Wu, Phys. Rev. B **96**, 035143 (2017).
[32] S. C. Miller and W. F. Love, *Tables of Irreducible Representations of Space Groups and Co-representations of Magnetic Space Groups* (Pruett, Boulder, CO, 1967).
[33] V. M. Goldschmidt, Naturwissenschaften **14**, 477 (1926).
[34] W. Zhong, D. Vanderbilt, R. D. King-Smith, and K. Rabe, Ferroelectrics **164**, 291 (1995).
[35] K. Momma and F. Izumi, J. Appl. Crystallogr. **44**, 1272 (2011).
[36] N. A. Pertsev, A. K. Tagantsev, and N. Setter, Phys. Rev. B **61**, R825(R) (2000).